Impact of CeO_x Additives on Cathode Catalyst Layer Poisoning

Dustin Banham[a], Siyu Ye[a], Tommy Cheng[a], Shanna Knights[a], S. Michael Stewart[b], and Fernando Garzon[c]

[a] Ballard Power Systems, 9000 Glenlyon Parkway, Burnaby, BC V5J 5J8, Canada
[b] Department of Chemical Engineering, University of New Mexico, Albuquerque, New Mexico
[c] Sensors and Electrochemical Devices, Los Alamos National Laboratory, Los Alamos, New Mexico

The impact of CeOx crystallite size on CeOx dissolution was investigated. Three CeOx additives were prepared having crystallite sizes of 6, 13, or 25 nm. An ex-situ method was developed to evaluate the chemical stability of these three CeOx samples, as well as one commercially available CeOx. It was determined that surface area, rather than crystallite size, is the best predictor of chemical stability. In-situ membrane electrode assembly (MEA) testing of the four CeOx additives demonstrated that prior to accelerated stress testing (AST), negligible dissolution of the CeOx additives occurs. Following AST cycling, it was found that end of life (EOL) performance was identical regardless of differences in total CeOx dissolution observed from the ex-situ testing. Finally, it was shown that increasing the anode RH during AST cycling leads to significantly higher EOL performance losses which was attributed to increased CeOx dissolution.

Introduction

Fuel cells are electrochemical devices capable of efficiently converting chemical energy into electrical energy while producing very little pollutants (e.g. NO_x, SO_x, particulates) (1). Due to their higher efficiency and cleaner operation vs. conventional internal combustion engines, fuel cells have become highly promising candidates for clean power generation. Much like a battery, PEMFCs contain an anode, a cathode and an electrolyte. The electrolyte dictates the required operating conditions of the fuel cell (temperature, pH, etc.), and thus fuel cells are classified according to the electrolyte that they employ. Currently, one of the most promising candidates for stationary, mobile, and automotive applications is the proton exchange membrane fuel cell (PEMFC), which utilizes a perfluorinated sulfonic acid (PFSA) polymer membrane (typically Nafion^{TM}). These membranes must be humidified with liquid water in order for facile proton conduction to occur, and thus PEMFCs typically operate at relatively low temperatures (60-85 ^{o}C).

While PFSA membranes are capable of achieving high proton conductivities (~ 10 S/m), they suffer from several modes of degradation during normal operating conditions (2). Of particular concern are the highly reactive free radicals ($OH^{\cdot}$, $OOH^{\cdot}$, $H^{\cdot}$) that are formed from the decomposition of H_2O_2 (an intermediate in the oxygen reduction reaction (ORR)) within the membrane (3-5). While H_2O_2 alone is not particularly damaging, the presence of

even trace amounts of Fenton's catalyst (e.g. Fe^{2+}/Fe^{3+}) greatly accelerates the decomposition of H_2O_2 into aggressive free radicals (6-8). These free radicals are known to attack PFSA membranes through an "unzipping" mechanism in which decomposition is initiated at one end of a PFSA unit and continues until complete decomposition into HF, CO_2 and low molecular weight compounds has occurred (3-5, 9). As a result of free radical attack, membrane thinning, and eventually complete failure (due to pinhole formation), can occur (3, 9).

In an effort to mitigate against free radical attack, recent work has focused on the incorporation of multivalent free radical scavengers in the form of salts (e.g. Ce^{3+}/Ce^{4+}, Mn^{2+}/Mn^{3+}) or metal oxides (e.g. CeO_x, MnO_x) into the membrane electrode assembly (MEA) (3-6). Specifically, it has been shown that by incorporating CeO_x into the MEA, membrane degradation (as measured by fluoride ion release) can be reduced by ~ 1000 x (vs. ~ 100 x for MnO_x) (5). While these results are highly promising, recent work by our group has indicated that during accelerated stress testing (AST), these metal oxides will dissolve, and the resulting cations will transport to the cathode catalyst layer (CCL) where they bind strongly with the $–HSO_3$ groups in the ionomer (6, 10). As this process occurs, the CCL ionic resistance is greatly increased due to the reduction in available $–HSO_3$ groups for proton conduction, and thus the performance of the PEMFC is significantly reduced. This effect is exacerbated once the cathode has degraded, as the reaction distribution shifts towards the cathode-GDL interface. Controlling the rate of CeO_x dissolution is therefore of great importance, as it may be possible to maintain sufficient Ce cations for free radical scavenging while minimizing the impact of these cations on the CCL.

Therefore, the goal of the present work has been to examine how several parameters (CeO_x crystallite size and anode relative humidity (RH)) impact on CeO_x dissolution during AST cycling. Four different CeO_x samples, each with a different crystallite size, were examined using an ex-situ method developed to screen the chemical stability of these materials. Following this, MEAs containing the CeO_x additives were prepared, and AST cycling was performed. Additionally, the impact of varying the anode RH during AST cycling was investigated.

Experimental

Synthesis of the CeOx Additives:

Ceria(III)acetate (Strem Chemicals) was dissolved in deionized water acidified to obtain a solution of approximated 0.1 M Ce^{3+}. Concentrated nitric acid (Fisher) was added until the ceria acetate had dissolved (pH = 1). 50% ammonium hydroxide solution (Alfa Aesar) was then added to the solution while it was manually agitated until the solution turned white and opaque (pH ~ 10). The solution was centrifuged, and then washed with DI water to remove acetate, ammonia, and nitric acid contaminants. This process was repeated three times. Samples were then dried in an oven at 140 °C for one hour to remove moisture. The dried samples were subsequently transferred to a ceramic boat and heated under air at 200, 600, or 800 °C for 1 h. The resulting samples are labeled as: LANL 200 ^oC, LANL 600 ^oC, and LANL 800 ^oC, since each of these samples were synthesized at Los Alamos National Laboratory.

Physical Characterization

The UV-visible spectroscopy was performed using a Hitachi U-2900 spectrophotometer and Hellma 10 mm cuvettes. All scans were performed from 250-600 nm. For the dissolution studies, each of the four CeOx samples were dispersed in 1 M H_2SO_4, and the samples were allowed to settle over night. UV-vis was performed the next day, and following this, the samples were heated at 50 ^oC for a period of three days, with UV-vis performed at the end of each day of heating. X-ray diffraction spectra were acquired using a D8ADVANCE X-ray diffractometer (Bruker Axs, Inc.) with a CuKα1 X-ray source scanning from 6 to 103◦ at an angle increment of 0.04◦/step. Gas sorption was performed with a Quantachrome Nova 2000e surface area and pore size analyzer. The specific surface area was obtained using a BET (Brunauer-Emmett-Teller) plot ($0.05 < P/Po < 0.30$), where P is the partial pressure of the adsorbate gas and Po is the vapour pressure of the adsorbate gas.

MEA Testing

For MEA testing, the CeOx additive loadings were 0.025, 0.012, or 0.006 mg/cm^2. The MEAs are referred to as MEA-LANL-X ^oC, where X is the calcination temperature used during the synthesis, with the exception of the MEA prepared form a commercial CeOx additive, which is labeled as MEA-Commercial-CeOx. All MEAs were composed of carbon-based gas diffusion layers (GDL) and Nafion membrane. The catalyst layers were comprised of 23 wt% Nafion with anode and cathode Pt catalyst loadings of 0.1 and 0.4 mg/cm^2, respectively. For MEA evaluation, research-scale test cells (active area of 50 cm^2) were used, and the operating conditions were 75 ^oC, 136 kPa, and 100% inlet RHs. Cathode AST cycling was performed at 80 ^oC and a pressure of 136 kPa. The cathode RH was held at 100 % while the anode RH was either 50 or 100 %. Potential cycling was performed with a lower potential limit (LPL) of 0.6 V and an upper potential limit (UPL) of 1.3 V. CO stripping cyclic voltammetry (CV) was performed in-situ to estimate the electrochemical catalyst surface area (ECSA) during beginning of life (BOL), middle of life (MOL) and end of life (EOL) testing. All CVs were obtained with CorrWare software using a PAR Model 263A potentiostat. During CV measurements, hydrogen and nitrogen were fed to the anode and cathode, respectively; with the anode thus acting as a dynamic hydrogen electrode (DHE) during CV measurements. Before each CO stripping experiment, the working electrode (cathode) was cleaned electrochemically three times by cycling from 0.1 to 1.2 V vs. DHE at a scan rate of 20 mV/s. The cathode was subsequently poisoned with 1.0% CO gas balanced with nitrogen, followed by purging with pure nitrogen. The CO stripping experiment was then carried out by scanning between 0.1 and 1.2 V vs. DHE at a scan rate of 20 mV/s. After each CO stripping CV, a blank scan in nitrogen between 0.1 and 1.2 V vs. DHE was also recorded for background correction and double-layer charging current (DLCC) measurements. In-situ electrochemical impedance spectroscopy (EIS) was also performed at BOL, MOL and EOL, using a Solartron SI 1287 potentiostat, Solartron SI 1255 frequency response analyzer, ZPlot/ZView software, and a transmission-line equivalent circuit. The EIS measurements were carried out at 0.45 V vs. DHE using an AC amplitude of 10 mV and a frequency range from 50000 to 0.5 Hz.

Results and Discussion

Three different CeOx samples were synthesized using a calcination temperature of 200, 600, or 800 ^{o}C. Following the synthesis, each of these samples was characterized by XRD (Fig. 1). Also shown in Fig. 1 is the XRD spectrum for a commercial CeOx sample.

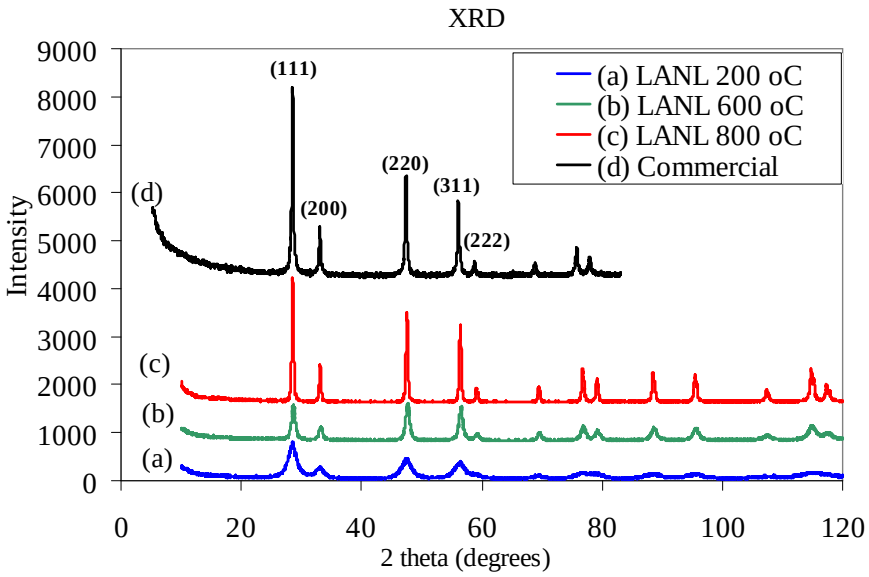

Figure 1: XRD spectra of the four CeOx samples.

The Scherrer equation was used to calculate the crystallite sizes from the XRD spectra (using the CeO_2 (111) peak), and the results are summarized in Table 1. Comparing among the LANL CeOx samples, it is clear that the crystallite size increases with the calcination temperature, as expected (11). While the synthesis conditions/approach for the commercial sample is not known, it was found to have a similar crystallite size to the LANL 800 ^{o}C sample.

Table I: Physical properties of the four CeOx samples.

Sample	Crystallite size (111) (nm)	BET Surface area (m^2/g)	Pore diameter (nm)	Micropore area (m^2/g)	Pore volume (mL/g)
CeO_x 200 ^{o}C	6	98	1.80	0	0.10
CeO_x 600 ^{o}C	13	30	1.85	0	0.06
CeO_x 800 ^{o}C	25	9	1.90	0	0.03
Commercial	30	55	12	0	0.12

Gas sorption analysis was performed on the four samples, and the isotherms are shown in Fig. 2. While all four isotherms are type IV, the commercial CeOx displays type H3 hysteresis whereas the LANL CeOx samples show type H4 (12). Both type H3 and type H4 hysteresis are characteristic of narrow, slit shaped pores, formed from non-rigid aggregates of primary particles. This suggests the porosity is from inter-particle pores as opposed to internal pores within the primary CeOx particles. Additionally, the primary difference between type H3 and H4 hysteresis is that type H4 occurs when the pores are primarily within the microporous (d < 2 nm) range (12). As can be seen from Table I, this observation

is supported by the measured pore diameters, which clearly show that the LANL CeOx samples all display maximum pore diameters < 2 nm, while the commercial CeOx is mesoporous ($2 \leq d \leq 50$ nm). However, despite the fact that the pores size distribution indicates that the LANL CeOx samples are mostly microporous, no measurable micropore surface area was detected. Together, this data suggests that while the LANL CeOx samples are largely non-porous, of the few pores that are present, most are in the micropore range. This is also supported by the low pore volumes measured for these samples.

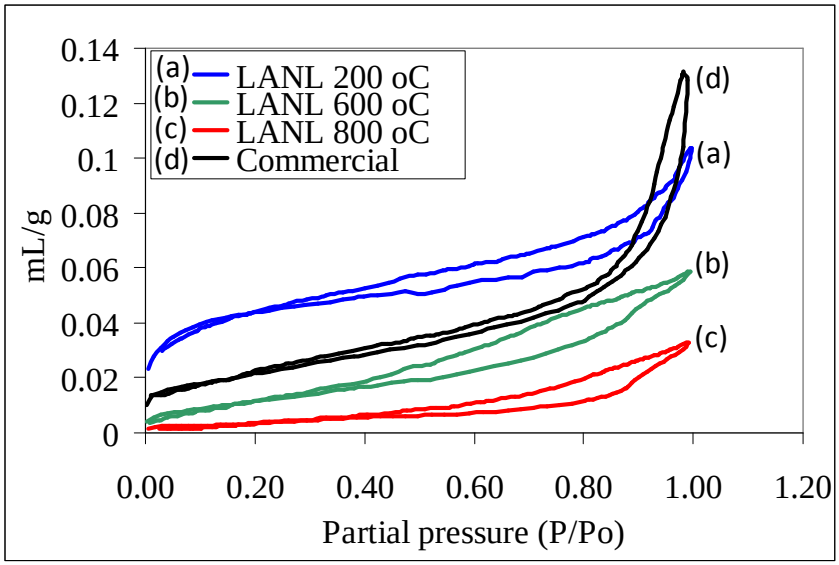

Figure 2. N_2 sorption isotherms for the four CeOx samples.

From the gas sorption data, it is possible to estimate the particle size of the CeOx samples using Eq. 1.

$$r = \frac{3000}{\rho \cdot \text{Surface Area}\left(\frac{m^2}{g}\right)} \qquad [1]$$

In Eq. 1, ρ is the bulk density of the sample and r is the particle radius. For this calculation to be accurate, the following four important assumptions must be true: 1) the samples contain no internal porosity, 2) the full external surface area is accessible to the adsorbate, 3) the density of the nanoparticle is equal to the bulk density of the material, and 4) the particles are either spherical or cubic. Assumption 1 and 2 are believed to be the most significant, and it is thus worth examining both in more detail.

Assumption 1 is expected to lead to an underestimation of particle size, since any internal porosity would enlarge the measured surface area thus decreasing the estimated particle radius. Based on the data in Table 1, assumption 1 appears valid for the LANL CeOx, but may not be valid for the commercial CeOx (which does appear to contain some internal porosity). It should be noted that internal porosity will also reduce the X-ray coherence length during the XRD measurement, which results in an underestimation of crystallite size. Conversely, assumption 2 leads to an overestimation of particle size, as any unmeasured surface area will result in a larger estimation of particle diameter (Eq. 1). Agglomeration of ceramic materials is very common, and thus it is highly unlikely that assumption 2 is completely correct for any of the CeOx samples. Due to this uncertainty, transmission

electron microscopy needs to be performed in order to verify the true particle sizes of these four samples.

Figure 3 compares the predicted particle size from gas sorption vs. the crystallite size from XRD. For the LANL samples, both the XRD and gas sorption data show the expected trend of increasing particle size with calcination temperature. However, the gas sorption data consistently predicts a larger particle size than does the XRD crystallite size, likely due to particle agglomeration. For the commercial sample, the particle size estimated from gas sorption is lower than that from XRD. As previously mentioned, this is likely due to some internal porosity in the commercial sample (Table 1), leading to an underestimation of particle diameter.

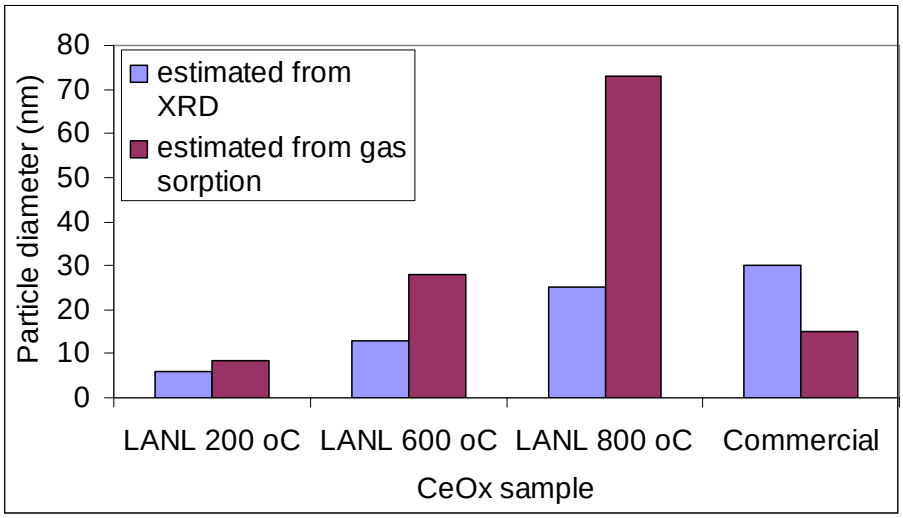

Figure 3. Gas sorption and XRD estimated particle sizes for the four CeOx samples.

To study the chemical stability of the CeOx samples, the samples were dispersed in 1 M H_2SO_4 and heated at 50 ^oC over a period of three days with periodic sampling for UV-visible spectroscopy. There were two goals from this study. The first was to determine the total amount of Ce cations released from each sample during the three day period. This is important as it provides an estimate of how quickly each CeOx sample would be expected to poison the CCL during MEA testing. The second goal was to determine the ratio of Ce^{3+}:Ce^{4+} released from each sample. This is of importance since it is believed that the ability/efficiency of Ce cations to scavenge free radicals may have a large dependence on the Ce^{3+}:Ce^{4+} ratio (4). Therefore, prior to monitoring the dissolution of the CeOx samples, it was crucial to first verify that UV-vis spectra of Ce^{3+}/Ce^{4+} solutions could be accurately deconvoluted such that the individual concentrations of Ce^{3+} and Ce^{4+} could be determined. However, it should be noted that any ratio of Ce^{3+}:Ce^{4+} that is measured ex-situ may not be representative of the true ratio within the MEA, where reducing conditions at the anode likely render most of the Ce cations in a 3+ oxidation state.

Two stock solutions of Ce^{3+} and Ce^{4+} were prepared, with concentrations of 1 mM and 0.1 mM respectively (the Ce^{4+} stock solution was 10 x more dilute vs. the Ce^{3+} solution due to the much stronger absorption of Ce^{4+} vs. Ce^{3+}). Three additional solutions were then prepared by mixing the stock solutions in a 3:1, 1:1, or 1:3 volume ratio, and UV-vis was performed on each of the solutions (Fig. 4). Two important observations are evident from Fig. 4. First, comparing the UV-vis spectra for the two stock solutions, it is clear that in 1 M H_2SO_4 Ce^{3+} and Ce^{4+} absorb at different wavelengths (Ce^{4+} = 320 nm, Ce^{3+} = 253 and 295

nm). Secondly, comparing the mixed Ce^{3+}/Ce^{4+} solutions, it is clear that the UV-vis spectra gradually change from Ce^{4+}-like to Ce^{3+}-like as the concentration of Ce^{3+} is increased vs. Ce^{4+}. Combined, these two observations suggest that deconvolution of a mixed Ce^{3+}/Ce^{4+} solution should be possible using UV-vis and stock solutions of Ce^{3+} and Ce^{4+}. This is confirmed by spectrum (f) in Fig. 4, which is a theoretical spectrum for a 3:1 Ce^{3+}:Ce^{4+} solution prepared from a 3:1 linear combination of spectra (e) and (a). As can be seen, spectra (d) and (f) perfectly overlap, clearly showing that deconvolution is possible and that this approach can be used to accurately calculate the respective concentrations of Ce^{3+} and Ce^{4+} in an unknown mixture of the two cations.

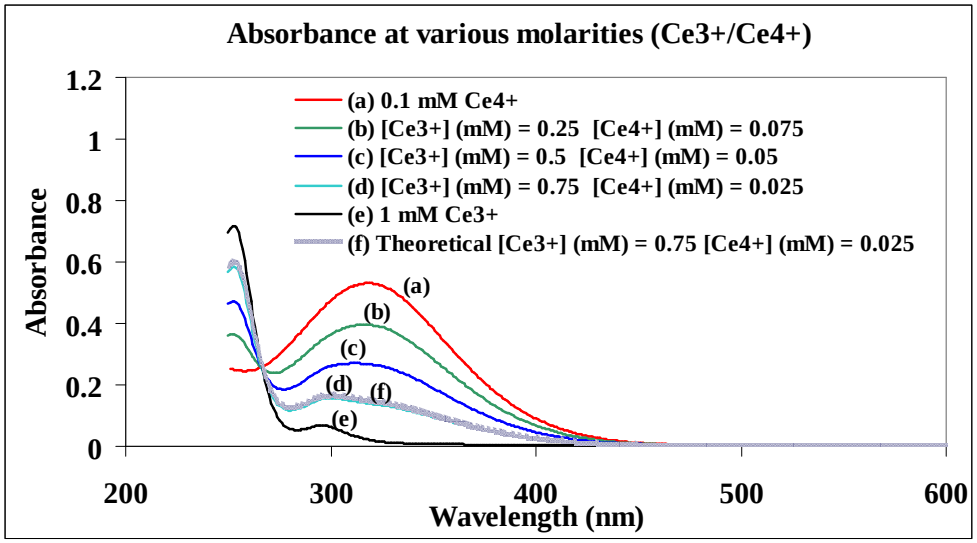

Figure 4. (a-e) UV-vis spectra for the five solutions of Ce^{3+}/Ce^{4+}. (f) Theoretical UV-vis spectrum for a linear combination of the Ce^{3+}/Ce^{4+} stock solutions in a 3:1 Ce^{3+}:Ce^{4+} ratio.

Figure 5 shows the concentration of Ce^{3+} and Ce^{4+} over the three days of heating. It is evident from Fig. 5 that calcination temperature has an impact on the stability of the LANL CeOx samples. It is also clear that crystallite size influences the ratio of Ce^{3+}/Ce^{4+} cations that are generated during dissolution of the CeOx samples.

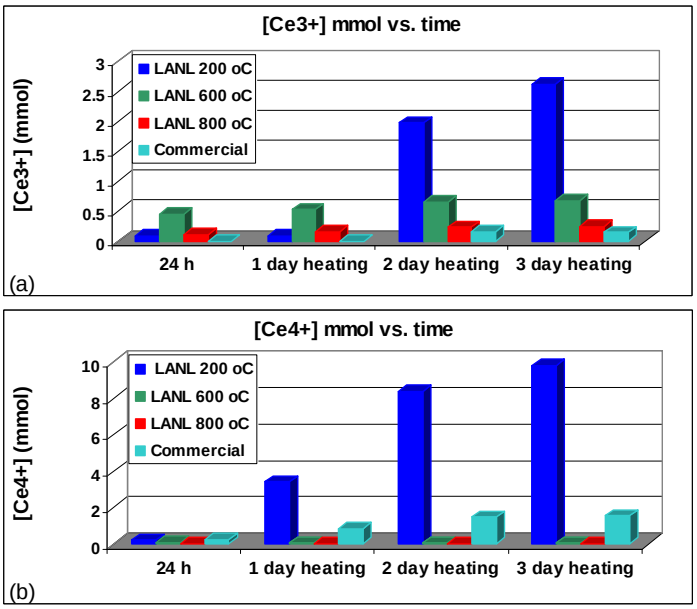

Figure 5. Concentration of (a) Ce^{3+} and (b) Ce^{4+} during the three days of heating as measured by UV-vis.

Based on the concentrations of the Ce^{3+}/Ce^{4+} ions, the total mass of CeOx that was dissolved can be calculated (Table 2). For this calculation, the Ce^{3+} was assumed to come from Ce_2O_3 dissolution and the Ce^{4+} was assumed to come from CeO_2 dissolution. It is clearly evident from Table 2 that, for the LANL CeOx samples, the total mass dissolved is a function of the calcination temperature.

Table II: Total mass dissolved after 3 days of heating at 50 °C for the four CeOx samples.

Sample	[Ce^{3+}] (mmol)	Mass Ce_2O_3 (mg)	[Ce^{4+}] (mmol)	Mass CeO_2 (mg)	Total Mass (mg)
LANL 200 °C	2.62	4.4	9.8	8.6	13
LANL 600 °C	0.84	4.4	0.046	0.16	4.6
LANL 800 °C	0.25	0.28	0.0038	0.0023	0.28
Commercial	0.14	0.94	1.57	5.4	6.3

The dissolution rate is expected to increase with increasing surface area because a larger exposed surface is available to react with the H_2SO_4. With decreasing crystallite size, the dissolution rate would also be expected to increase for two reasons. If the crystallite size is representative of the particle size, then decreasing crystallite size should correlate with a smaller particle size, and thus a larger percent of exposed surface atoms to react with the H_2SO_4. Additionally, the percentage of Ce_2O_3 at the surface of the particle increases with decreasing crystallite size (13, 14), and Ce_2O_3 is known to be less stable in acidic solutions than CeO_2 (15). In order to determine whether BET surface area or XRD crystallite size is the best predictor of chemical stability, both parameters were plotted against the total mass dissolved for each of the four CeOx samples (Fig. 6).

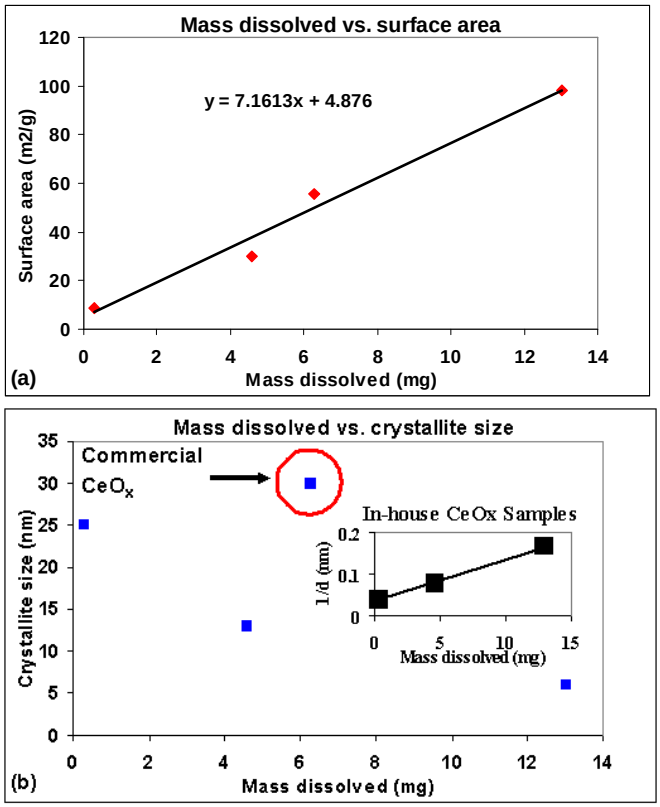

Figure 6. (a) Surface area (m^2/g) and (b) crystallite size (nm) of the four CeOx samples vs. the total mass dissolved over three days.

From Fig. 6 (a) it is clear that there is a linear trend between the measured surface area and the total mass dissolved, as would be expected. Fig. 6 (b) shows that, when comparing among the LANL CeOx samples, the expected trend of increasing dissolution with decreasing crystallite size is observed. If the trend in Fig. 6 (b) is due to differences in specific surface area (due to differences in crystallite size) a plot of 1/d (where d is crystallite size) vs. mass dissolved should be linear. This is because specific surface area has a 1/d dependence (Eq. 1), and the mass dissolved was already shown to have a linear dependence on surface area (Fig. 6 (a)). This is precisely what is observed when such a plot is prepared for the LANL CeOx samples (Fig. 6 (b) inset). The commercial CeOx does not fit this trend, and shows a much larger amount of dissolution than would be expected based on the other CeOx samples (Fig. 6 (b)). This is almost certainly due to the fact that the commercial CeOx has a larger internal porosity vs. the other CeOx materials, since any internal porosity would increase the exposed surface area resulting in a larger amount of dissolution vs. a non-porous sample of the same crystallite size.

The ex-situ characterization clearly indicates that dissolution of the CeOx samples can occur in the absence of any applied potential. Therefore, prior to performing any AST, it was crucial to first determine whether dissolution would occur during conditioning of the MEAs containing CeOx. Two conditioning times (24 h and 60 h) were evaluated for MEA-LANL-800^{o}C, with Fig. 7 (a) showing that no difference in BOL performance was observed. Additionally, Fig. 7 (b) indicates that BOL performance is independent of crystallite size or CeOx loading. Combined, the data in Fig. 7 suggests that any initial dissolution of the CeOx has a negligible impact on BOL performance.

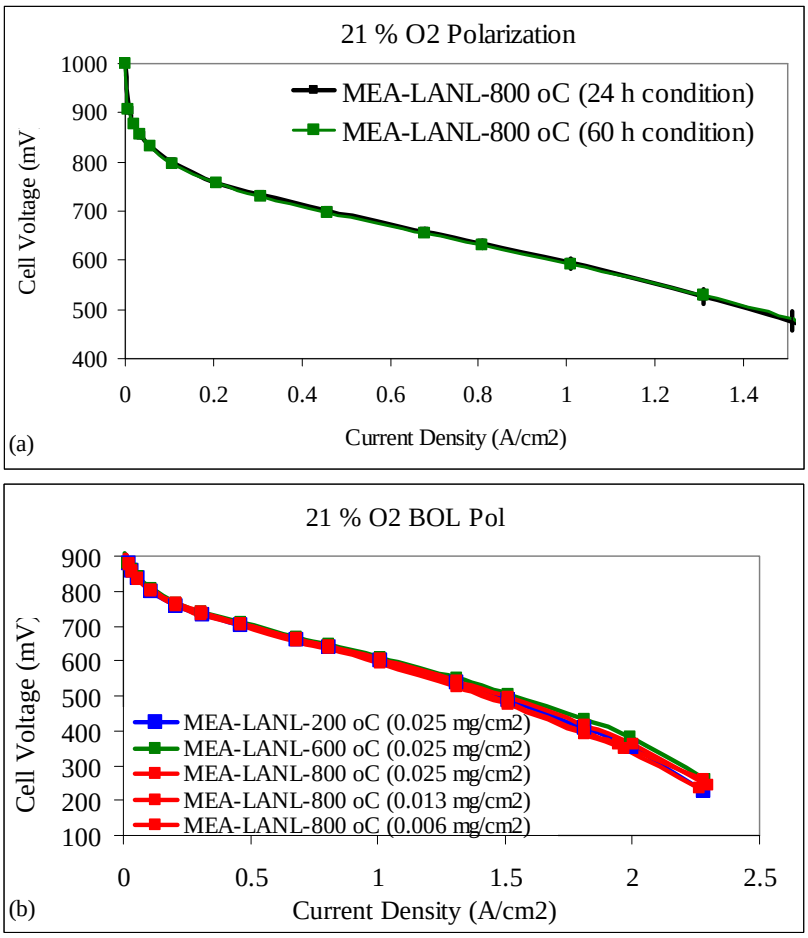

Figure 7. (a) Impact of conditioning time on BOL performance and (b) impact of crystallite size and loading on BOL performance (after 24 h of conditioning). Temperature: 75 ^{o}C, Pressure: 136 kPa, Inlet RH: 100 %, Fuel/oxidant: H_2/Air.

AST cycling was performed on MEA-LANL-800^{o}C, since the ex-situ testing had indicated that the LANL-800 ^{o}C CeOx sample was the most stable of the CeOx additives. For comparison, AST cycling was also performed on MEA-Commercial-CeOx and a baseline MEA containing no CeOx. Fig. 8 (a) shows that, compared to the baseline MEA, both MEA-LANL-800^{o}C and MEA-Commercial-CeOx show significantly lower EOL performance. The lower performance of MEA-Commercial-CeOx vs. the baseline MEA is not surprising, and the mechanism for this large EOL performance loss has previously been examined by group (6). However, the fact that MEA-LANL-800^{o}C has identical EOL performance loss, despite showing ~ 20 x less dissolution during the ex-situ testing (Table 2) was unexpected. It is known that cationic contaminants will readily accumulate in the cathode catalyst layer (CCL) (10). Therefore, a possible explanation for the identical EOL performance of these two MEAs is that once the CCL reaches a saturation level of Ce cations, no further poisoning can occur. At the loadings used for this study (0.025 mg/cm^2), it is possible that the CCL becomes saturated even for the LANL-800 ^{o}C CeOx, and thus any further dissolution of the commercial CeOx vs. the LANL-800 ^{o}C CeOx is irrelevant. Performing AST cycling at lower additive loadings will be required to verify this hypothesis.

In order to further examine the factors leading to dissolution of the CeOx, the impact of anode RH during AST cycling was also investigated. As is shown in Fig. 8 (b), reducing

the anode RH to 50 % during AST cycling greatly improves EOL performance. This result highlights the significance of H_2O in the dissolution mechanism of CeOx, and may provide a key insight into future strategies for reducing CeOx dissolution.

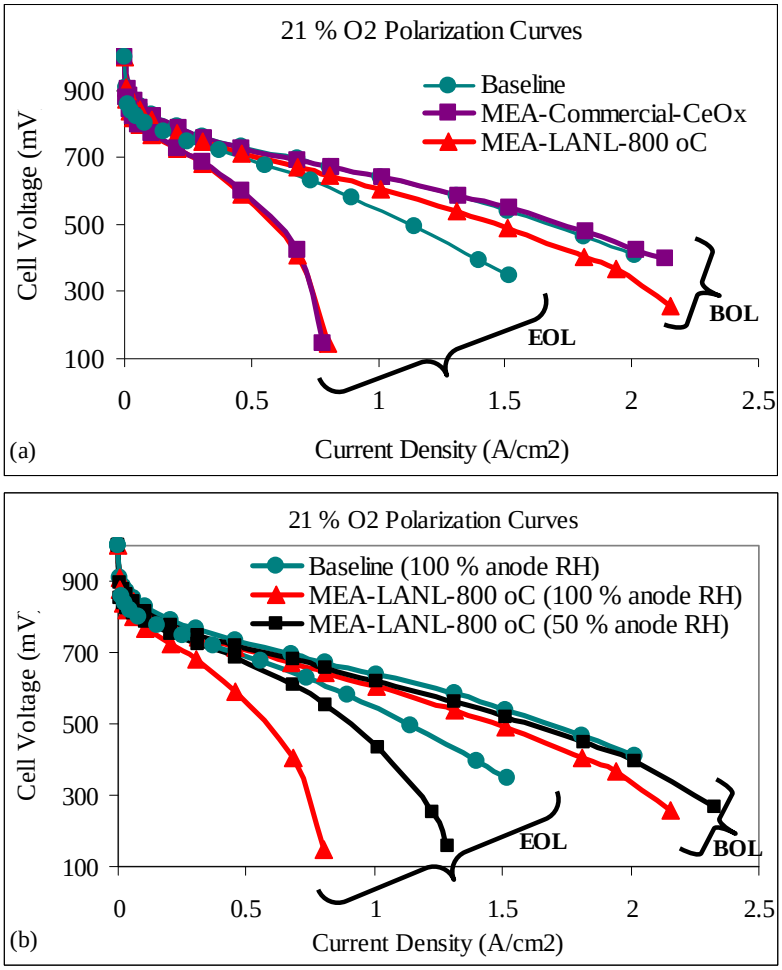

Figure 8. (a) BOL and EOL performance for MEA-LANL-800 ^{o}C, MEA-Commercial-CeOx, and a baseline MEA. (b) BOL and EOL performance for MEA-LANL-800 ^{o}C and a baseline MEA, showing the impact of anode RH during AST cycling on EOL performance. Temperature: 75 ^{o}C, Pressure: 136 kPa, Inlet RH: 100 %, Fuel/oxidant: H_2/Air. For (b), anode RH values of 50 % and 100 % were examined during AST cycling. All CeOx additive loadings were 0.025 mg/cm^2.

Conclusions

The impact of CeOx crystallite size, and anode relative humidity during accelerated stress testing (AST), on membrane electrode assembly (MEA) end of life (EOL) performance was examined. CeOx samples were prepared using three different calcination temperatures (200, 600, and 800 ^{o}C), leading to crystallite sizes of 6 (LANL-200 ^{o}C), 13 (LANL-600 ^{o}C), or 25 (LANL-800 ^{o}C) nm. A method for monitoring ex-situ chemical stability was developed, and used to characterize the three LANL CeOx samples, as well as one commercial CeOx. The chemical stability was found to increase in the following order: LANL-200^{o}C < Commercial < LANL-600^{o}C < LANL-800 ^{o}C. Following the chemical stability tests, each of the four CeOx samples were evaluated in-situ. MEA beginning of life (BOL) performance

demonstrated no dependence on conditioning time, crystallite size, or loading of the CeOx additives suggesting that any initial dissolution of CeOx has a negligible impact on performance. Finally, anode RH (during AST cycling) was found to have a major impact on EOL performance, with higher anode RHs resulting in significantly more severe EOL losses, likely due to increased CeOx dissolution.

Acknowledgments

We gratefully acknowledge the U.S. Department of Energy, Office of Fuel cell Technologies, for financial support, and the Natural Sciences and Engineering Research Council of Canada (NSERC) for the scholarship support of DB. The authors also thank Alan Young for many helpful discussions.

References

1. F. Barbir, *PEM Fuel Cells: Theory and Practice*, Elsevier Academic Press (2005).
2. Y. Sone, P. Ekdunge and D. Simonsson, *Journal of The Electrochemical Society*, **143**, 1254 (1996).
3. B. P. Pearman, N. Mohajeri, D. K. Slattery, M. D. Hampton, S. Seal and D. A. Cullen, *Polymer Degradation and Stability* (2013).
4. L. Gubler and W. H. Koppenol, *Journal of The Electrochemical Society*, **159**, B211 (2011).
5. F. D. Coms, H. Liu and J. E. Owejan, *ECS Transactions*, **16**, 1735 (2008).
6. T. T. H. Cheng, S. Wessel and S. Knights, *Journal of The Electrochemical Society*, **160**, F27 (2013).
7. H. Li, K. Tsay, H. Wang, J. Shen, S. Wu, J. Zhang, N. Jia, S. Wessel, R. Abouatallah, N. Joos and J. Schrooten, *Journal of Power Sources*, **195**, 8089 (2010).
8. L. Gubler, S. M. Dockheer and W. H. Koppenol, *Journal of The Electrochemical Society*, **158**, B755 (2011).
9. R. Borup, J. Meyers, B. Pivovar, Y. S. Kim, R. Mukundan, N. Garland, D. Myers, M. Wilson, F. Garzon, D. Wood, P. Zelenay, K. More, K. Stroh, T. Zawodzinski, J. Boncella, J. E. McGrath, M. Inaba, K. Miyatake, M. Hori, K. Ota, Z. Ogumi, S. Miyata, A. Nishikata, Z. Siroma, Y. Uchimoto, K. Yasuda, K.-i. Kimijima and N. Iwashita, *Chemical Reviews*, **107**, 3904 (2007).
10. B. Kienitz, B. Pivovar, T. Zawodzinski and F. H. Garzon, *Journal of The Electrochemical Society*, **158**, B1175 (2011).
11. F. Zhang, S.-W. Chan, J. E. Spanier, E. Apak, Q. Jin, R. D. Robinson and I. P. Herman, *Applied Physics Letters*, **80**, 127 (2002).
12. S. Lowell, J. E. Shields, M. A. Thomas and M. Thommes, *Characterization of Porous Solids and Powders: Surface Area, Pore Size and Density*, p. 347, Springer, Dordrecht, Netherlands (2006).
13. A. Karakoti, S. Singh, J. M. Dowding, S. Seal and W. T. Self, *Chemical Society Reviews*, **39**, 4422 (2010).
14. S. Tsunekawa, K. Ishikawa, Z. Q. Li, Y. Kawazoe and A. Kasuya, *Physical Review Letters*, **85**, 3440 (2000).
15. D. R. Ou, T. Mori, K. Fugane, H. Togasaki, F. Ye and J. Drennan, *The Journal of Physical Chemistry C*, **115**, 19239 (2011).